



Effects of heterogeneous gouge segments on the slip behavior of experimental faults at dm scale



L. Buijze^{a,b,*}, Y. Guo^c, A.R. Niemeijer^a, S. Ma^c, C.J. Spiers^a

^a High Pressure Temperature Laboratory, Department of Earth Sciences, Utrecht University, the Netherlands

^b Applied Geosciences, Energy Transition, TNO, the Netherlands

^c State Key Laboratory of Earthquake Dynamics, Institute of Geology, China Earthquake Administration, Beijing, China

ARTICLE INFO

Article history:

Received 20 December 2019

Received in revised form 15 September 2020

Accepted 28 October 2020

Available online 27 November 2020

Editor: J.-P. Avouac

Keywords:

heterogeneous fault friction

unstable sliding

slow slip

velocity-weakening asperity

scaled experiments

confined rupture

ABSTRACT

Frictional heterogeneity within fault zones is one of the factors proposed to explain the spectrum of slow, intermediate, and fast slip behaviors exhibited by faults in nature. Numerical modeling shows how even a simplified model setup incorporating sliding on a velocity-weakening (VW) patch surrounded by velocity-strengthening (VS) material can reproduce a rich variety of slip behaviors resembling nature. However, experimental investigations of sliding on heterogeneous faults are few. In this study, the slip behavior of three, 347 mm long \times 50 mm wide, heterogeneous experimental faults, constructed using diagonally sawcut PMMA forcing blocks, was investigated at low normal stresses (<10.5 MPa) and room temperature. Fault friction was controlled by including an 80 mm long, 2 mm thick, central segment of VW gypsum “gouge” flanked by two VS segments composed of calcite, quartz, or kaolinite. The length of the VW segment was of the same order or just below the critical nucleation length for gypsum gouge. Strain gauges and multi-rate digital imaging were used to map stress and displacement along the fault zone. At the highest normal stress the data showed confined ruptures, whereby rupture nucleated in the VW gypsum and was arrested or strongly decelerated in the VS segments. Slip rates on the VW segment were close to dynamic slip rates, but significant slow slip was also observed in the VW segment between rapid events. Lowering the normal stress on the fault, from 10.5 to 1 MPa resulted in slow slip events occurring uniformly over the whole fault (calcite–gypsum fault), near-stable sliding on the whole fault (quartz–gypsum fault), or persistent stick-slip behavior on the VW segment as at higher normal stress (kaolinite–gypsum fault). The spectrum of behaviors observed is consistent with that predicted by previous numerical modeling of frictionally heterogeneous faults with a similar geometry as the experiment. The experiments also showed how stress concentrations influence slip behavior. Specifically, normal stress concentrations, formed due to heterogeneous compaction of the kaolinite and VW gypsum gouges, promoted unstable sliding in the latter. Shear stress concentrations at the extremities of the VW segment caused significant slow slip to occur at the extremities of the VW segments, and in the quartz–gypsum experiment seemed to promote local slip events at low stresses. The observed fault slip behavior was thus controlled by gouge friction and stress distribution, and is consistent with numerical models and theory as applied to both natural and induced seismicity.

© 2020 The Author(s). Published by Elsevier B.V. This is an open access article under the CC BY license (<http://creativecommons.org/licenses/by/4.0/>).

1. Introduction

Observations from dense seismological monitoring networks and geodetic monitoring reveal a rich variety of slip behaviors in plate-boundary faults. Besides ‘regular’, fast earthquakes and megathrust events, slower phenomena such as slow slip events,

episodic tremors or low frequency events, and very low frequency VLF earthquakes have been observed in subduction zones in Japan (Ito et al., 2007; Obara et al., 2004), Cascadia (Schmidt and Gao, 2010) and in New Zealand (Wallace et al., 2016), as well as on the San Andreas fault (Linde et al., 1996). The duration of these events is orders of magnitude larger than the duration of regular earthquakes of comparable seismic moment and ranges from seconds to years (Peng and Gomberg, 2010). Interestingly, different slip behaviors can occur simultaneously and at the same location on individual faults. For example, slow slip events are often accom-

* Corresponding author at: Applied Geosciences, Energy Transition, TNO, Princenlaan 6, 3584 CB Utrecht, the Netherlands.

E-mail address: loes.buijze@tno.nl (L. Buijze).

panied by tremors (Ito et al., 2007; Obara et al., 2004), and given fault segments can sometimes rupture in both fast and slow modes (Veedu and Barbot, 2016).

Slow slip phenomena are not limited to plate boundary faults but have also been inferred on smaller scale crustal faults, in association with induced earthquakes. Long-period, long-duration events recorded during densely monitored hydraulic fracturing stimulations have been attributed to slow fault slip (Das and Zoback, 2013; Kumar et al., 2019), though the origin of (some of) these events is debatable (Zecevic et al., 2016). In addition, during in-situ injection experiments on a decametric scale, Derode et al. (2015) observed both tremors and long-period events, in addition to aseismic slip and 'regular' microseismicity. Though difficult to image on smaller scale faults, slow and fast slip phenomena may thus play an important role in the faulting process, both for natural and induced fault slip.

One explanation commonly cited for the observed variety of fault slip behaviors is the heterogeneous nature of fault zones (e.g. Barbot, 2019; Luo and Ampuero, 2018; Skarbek et al., 2012). Geological observations on exhumed fault zones show that fault zone lithology is heterogeneous over a broad range of length scales (Fagereng and Sibson, 2010). Fault zones often contain lenses of rigid, brittle material derived from the host rock which are surrounded by a weaker phyllosilicate-rich matrix (Collettini et al., 2011; Faulkner et al., 2003). The juxtaposition of contrasting lithologies along offset faults also results in spatially varying fault rock composition (Tesei et al., 2014), which is especially important on faults cross-cutting layered (sedimentary) sequences. Different fault rock lithologies translate into different mechanical properties, e.g. different frictional strengths and varying slip- and velocity-dependences thereof. In addition, different lithologies and their specific hydrogeological properties, as well as geometrical variations and irregularities within the fault zone, translate into varying fluid pressures and/or stress state along faults (e.g. Schmittbuhl et al., 2006).

Conceptually, the varying mechanical properties along fault zones are often represented as asperities, which are competent and/or have velocity-weakening (VW) frictional properties so they can slip unstably, surrounded by (often less competent) matrix material which is velocity-strengthening (VS) and slides stably (e.g. Ito et al., 2007). Numerical modeling studies using rate-and-state friction, with one or multiple (interacting) asperities, have successfully reproduced some of the slip phenomena observed in plate boundary faults, including slow slip earthquakes and migrating tremors (Ariyoshi et al., 2009; Luo and Liu, 2019a), small-scale (repeating) earthquakes (Chen and Lapusta, 2009; Schaal and Lapusta, 2019), alternating slow and fast events (Veedu and Barbot, 2016) and megathrust events (Shibazaki et al., 2011). Even a single-asperity fault (a VW segment flanked by VS segments) can generate a wide variety of fast and slow slip behaviors, comparable to the variability observed in nature (e.g. Barbot, 2019; Luo and Ampuero, 2018; Skarbek et al., 2012). Key parameters controlling slip behavior are the size of the asperity with respect to the critical nucleation size, the relative magnitude of the velocity-weakening versus velocity-strengthening properties, the fraction of VW material on the fault, as well as the normal stress on the different segments. In the laboratory, slow slip behavior has also been observed on frictionally homogeneous faults where the length of the experimental fault was close to the critical nucleation length (McLaskey and Yamashita, 2017), or the stiffness was close to the critical stiffness (Leeman et al., 2016). In an experimental study by Ma and He (2001) sliding on a frictionally heterogeneous fault in a double direct shear setup was investigated, where a 40 or 80 mm long and 1 mm thick plaster (gypsum) segment was present in the center of a 300 mm long granodiorite fault surface. The strain data revealed spatially heterogeneous stress build-up and release along the fault,

as well as an alternation of smaller and larger events in which part of or all the fault ruptured (Ma and He, 2001). However, further experimental evidence on the sliding behavior on frictionally heterogeneous faults is lacking.

Densely instrumented dm- to m-scale experiments offer the opportunity to study the nucleation of unstable slip and the propagation of the instability (e.g. Ma and He, 2001; e.g. McLaskey and Yamashita, 2017; McLaskey and Kilgore, 2013; Ohnaka et al., 1986; Okubo and Dieterich, 1981; Zhuo et al., 2018). Here, a 347 mm long fault was used to investigate the effect of frictional heterogeneity on the slip behavior using a single-asperity fault as also used in modeling (e.g. Luo and Ampuero, 2018). Different gouge materials were used to create the heterogeneous frictional properties along the fault. Compliant polymethylmethacrylate (PMMA) forcing blocks were used to reduce the critical nucleation length. At the initial stresses applied, the length of the VW segment was close to the nucleation length identified from similar uniform fault experiments (Buijze et al., 2020). During the experiments, the applied stress was varied to change the nucleation length. We evaluate the sliding behavior of these heterogeneous faults at the different loading conditions imposed, and compare our observations with the sliding behaviors predicted by previous theoretical and/or numerical modeling studies.

2. Methods

Four experiments on 347×50 mm sawcut experimental faults sandwiched by PMMA forcing blocks were performed in a horizontal biaxial machine located at the Institute of Geology, China Earthquake Administration in Beijing (Zhuo et al., 2018; Buijze et al., 2020). The experiments were conducted under low normal stresses (<10.5 MPa) and at room temperature. In one experiment the fault lithology was homogeneous, whereas in three experiments fault zone lithology was heterogeneous (Fig. 1).

2.1. Fault gouge materials and fault composition

Four different types of fault gouge with different frictional strengths and velocity-dependence were used to control the properties along the (heterogeneous) large-scale experimental faults. Gypsum gouge was obtained by sieving crushed natural gypsum from Somerset U.K. (de Meer and Spiers, 1997) to <150 μm (Buijze et al., 2020). Furthermore calcite gouge was used with a grain-size 120–150 μm , and pure quartz powder (Fluka Chemika, no. 83340) was used with a grain-size <63 μm , and median grain size of 20 μm . The fourth fault gouge material was kaolinite (Aldrich, CAS no. 1332-58-7) with a median grain size of 5 μm .

The intrinsic frictional properties and sliding behavior of these four gouges are summarized in Table 1 (Supplementary Information S1). Gypsum had the highest frictional strength, followed by quartz and calcite, and kaolinite was significantly weaker than the other three gouges. Triaxial experiments on gypsum gouge showed persistent stick-slip behavior at normal stresses <20 MPa at displacements <10 mm (Fig. S1). Velocity steps on gypsum gouge in a rotary shear apparatus at normal stresses between 2 and 10 MPa, displacements 9–50 mm, and velocities between 5–100 $\mu\text{m/s}$ yielded an average $a - b$ of -0.0031 and D_c of 1.7 μm (Fig. S2, Buijze et al., 2020). Velocity steps on gypsum gouge deformed at 10–14 MPa normal stress, displacements of 20–25 mm, and velocities of 100–1000 $\mu\text{m/s}$ in a biaxial apparatus yielded similar rate-and-state (RSF) parameter $a - b$ of -0.002 to -0.005 (Fig. S2, C. Marone, pers. comm). It is assumed the RSF parameters of gypsum do not change significantly with displacement and are similar at the displacements relevant to the large-scale experiments in this study (4–12 mm). The other three gouges were velocity strengthening to neutral (Carpenter et al., 2016; Ikari et

Table 1

Average frictional properties of the four gouges materials used to control fault friction. The parameters were obtained by averaging values obtained from various friction experiments in different apparatuses, at a normal stress <20 MPa and ambient humidity or 100% relative humidity. See also Supplementary Information 1.

	μ	a	b	$a - b$	D_c (μm)
Calcite	0.63	0.0084 ± 0.0064	0.0074 ± 0.0064	0.0009 ± 0.002	82.0 ± 11.4
Quartz (disp < 10 mm)	0.67	0.0088 ± 0.0024	0.0064 ± 0.0036	0.0024 ± 0.0026	19.2 ± 13.8
Quartz (disp > 10 mm)	0.67	0.0073 ± 0.0021	0.0083 ± 0.0019	$9 \cdot 10^{-4} \pm 0.001$	24.2 ± 25.7
Kaolinite	0.31	0.0038 ± 0.0018	0.00094 ± 0.0031	0.0048 ± 0.0015	62.8 ± 109.5
Gypsum	0.8–1	0.0053 ± 0.0039	0.0084 ± 0.01	-0.0031 ± 0.0032	2.4 ± 1.7

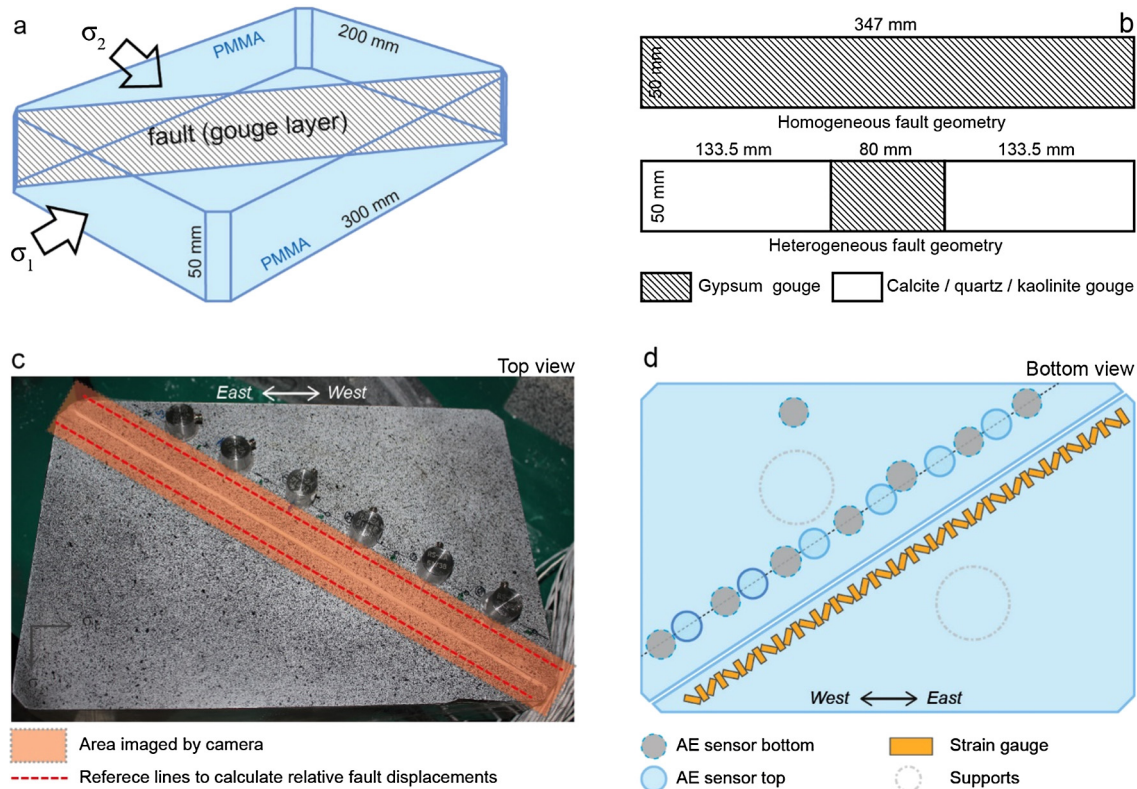


Fig. 1. Sample assembly and instrumentation. a) PMMA forcing blocks, fault gouge layer, and principal horizontal stresses applied by a horizontal biaxial deformation apparatus. b) Fault gouge lithology for a homogeneous gypsum gouge fault and a heterogeneous fault. c) Top view of the sample assembly and the area imaged by a camera suspended above the sample assembly. d) Bottom view of the sample assembly showing the positioning and orientation of the single-component strain gauges along the fault zone. (For interpretation of the colors in the figure(s), the reader is referred to the web version of this article.)

al., 2016; Mair and Marone, 1999, Baden, pers. comm, Hunfeld, pers. comm., Niemeijer, pers. comm.). Kaolinite is most velocity-strengthening, followed by quartz (at displacements <12 mm), and calcite which is only weakly velocity strengthening (Fig. S2, Table 1). The velocity dependence of quartz decreases with displacement, and becomes velocity neutral to velocity weakening at shear displacements exceeding 10 mm. Note that for all gouges the scatter in $a - b$ is significant.

2.2. Sample assembly, loading apparatus, and experimental procedure

Two PMMA forcing blocks formed a rectangular sample assembly of $300 \times 200 \times 50$ mm, with a vertical fault of 347×50 mm along the diagonal (Fig. 1a). The fault surfaces were prepared by grinding with #80 SiC powder. A 2 mm thick wet gouge layer was pasted evenly along the fault surface and left to dry, and subsequently left to equilibrate in an enclosed container in the presence of a saturated NaCl solution (relative humidity 75%). The second PMMA block was placed on top of the gouge layer and tape was placed along the fault ends and bottom margin. The sample assembly was then rotated and placed in the biaxial loading frame (Zhuo

et al., 2018; Buijze et al., 2020). After a pre-compaction phase (with $\sigma_1 = \sigma_2 = 15$ MPa for 5–10 min) σ_1 and σ_2 were lowered to 5 MPa. Shearing was initiated by imposing a constant displacement rate of $5 \mu\text{m s}^{-1}$ in the σ_1 -direction whilst keeping σ_2 constant at 5 MPa. After 3.5 mm of load point displacement d_1 the displacement rate was decreased to $1 \mu\text{m s}^{-1}$. During the experiment σ_2 was stepped down in various stages to a minimum of 0.3 MPa, and then stepped up again so that the sliding behavior under different normal stresses could be investigated. Note that the effect of cumulative displacement was not investigated independently; in the discussion section the effect of displacement on the frictional behavior is addressed.

2.3. Instrumentation and data processing

Two load cells were used to measure the loads applied to the sample assembly, which were converted into principal stresses σ_1 and σ_2 (Fig. 1a). These stresses were translated to the macroscopic shear stress τ^* and macroscopic normal stress σ_n^* along the fault plane, the ratio of which gives the macroscopic friction coefficient $\mu^* = \tau^*/\sigma_n^*$. Two linear variable displacement transducers (LVDTs)

were used to measure the macroscopic displacement in the σ_1 - and σ_2 -directions, d_1 and d_2 . The macroscopic shear displacement along the fault is expressed as $d_t^* = d_1 / \cos \theta \approx 1.2d_1$. Both the loads and the load point displacements were recorded continuously at 1 kHz.

46 single-component metal foil resistance strain gauges (9×4.5 mm) were glued to one of the PMMA forcing blocks along the fault's bottom margin at 10 mm from the fault. Strains were recorded continuously at 500 kHz, with a maximum resolvable frequency of 50–100 kHz (Buijze et al., 2020). The gauges formed 22 rectangular rosettes labeled SG24 through SG316, with the number indicating the distance from the eastern fault end in mm (Fig. 1d). These rosettes give the local 2D strain tensor, which is converted to local shear stress τ , local normal stress σ_n , and the local stress ratio τ/σ_n along the fault. For slip events the stress drop $\Delta\tau$ was defined as the difference in shear stress 0.1 s before and after the event. The shear stress evolution during fast slip was also fitted with an exponential function to obtain a characteristic duration and strength drop (Supplementary Information S2, Fig. S3).

The top surfaces of the PMMA blocks were painted white with a black speckle pattern (Fig. 1c). An area of $\sim 350 \times 39$ mm (2048×228 pixels, 1 pixel = 0.171 mm) centered around the fault zone was imaged with a Photron Fastcam SA2 high speed camera which was suspended above the sample. Images were acquired throughout the experiment at 1 fps, and at 5000–9000 fps for a number of selected time periods or slip events. Full coverage of the experiment was not possible, as the camera cannot acquire new images during times when data is transferred from the camera's memory to the PC. Digital Image Correlation (DIC) using PIVlab v2.02 (Thielicke and Stamhuis, 2014) was used to obtain the fault-parallel or fault-normal displacements at different stages during the experiment. To compute the relative fault-normal displacement d_n (positive is compaction) and fault-parallel or shear displacement d_t (positive is left-lateral motion) respectively the normal and shear displacements at opposing points along two lines parallel to the fault zone at a distance of 10 mm from the fault were subtracted (Zhuo et al., 2018). Average shear displacements for the three segments are denoted with d_{tVW} , d_{tVS1} , and d_{tVS2} . We also define the maximum shear slip rate v averaged over the different segments (e.g. v_{VWmax}) as the largest difference in d_{tVW} per frame time increment. The rupture length was defined as the fault length that slipped with an amount larger than the noise level ($> 5 \mu\text{m}$).

3. Results

3.1. Mechanical data at different confining stresses for the four fault compositions

Fig. 2 shows the relative macroscopic shear stresses τ^* during shearing of the four fault compositions at different confining stresses σ_2 (for full experiment see Fig. S4).

Stick-slip behavior was observed for the gypsum fault at all the σ_2 conditions evaluated (see also Buijze et al., 2020). The macroscopic stress drop $\Delta\tau^*$ decreased with confining stress from 0.4 MPa ($\sigma_2 = 5$ MPa) to 0.1 MPa ($\sigma_2 = 0.3$ MPa), and the recurrence interval decreased from 100 s to 10 s (Fig. 2a).

Stick-slips were also observed for sliding on the heterogeneous faults at $\sigma_2 = 5$ MPa, but the size of the stick-slips was significantly smaller than for the homogeneous gypsum fault (Fig. 2b-d). Macroscopic stress drops ranged from 0.05 MPa (calcite-gypsum fault) to 0.1 MPa (kaolinite-gypsum fault), and recurrence times were 20–35 s. At lower σ_2 markedly different sliding behaviors were observed for the three different heterogeneous fault compositions. For the calcite-gypsum fault, the stick-slips changed into slow slip events ($\sigma_2 = 1.2$ MPa) with recurrence time of 30–40 s (Fig. 2f). At the lowest σ_2 of 0.3 MPa the duration of the slow slip

increased to ~ 20 s, with a recurrence time of 40–50 s (Fig. 2j). For the quartz-gypsum fault the stick-slips became smaller and more irregular ($\sigma_2 = 1.2$ MPa) with recurrence times of 5–10 s, and could no longer be recognized at the lowest confining stress ($\sigma_2 = 0.3$ MPa) (Fig. 2k). For kaolinite-gypsum on the other hand, stick-slips persisted over the entire range of confining stresses (Fig. 2l). So even though the confining stresses and the properties of the velocity-weakening gypsum segment are the same for all the three heterogeneous fault experiments, the combination with different velocity-strengthening gouges resulted in different sliding modes with decreasing σ_2 . For the gypsum fault, calcite-fault, and the kaolinite-gypsum fault, the observed sliding behaviors are largely recoverable as the normal stress is stepped back up, indicating that the slip behavior does not change significantly with progressive displacement (Fig. 2q, s). For the quartz-gypsum fault on the other hand, the sliding behavior changes with displacement; during the second load stage at $\sigma_2 = 5$ MPa large stick-slip events were observed of comparable magnitude as those of the gypsum fault, superimposed with smaller, shorter duration stick-slip cycles (Fig. 2r).

3.2. Local stresses along the fault and shear displacements

The slip events observed in the macroscopic stress data at $\sigma_2 = 5$ MPa are also clearly visible in the local stress measurements and image data (Fig. 3). These data reveal that the fault length that slipped during instability (rupture length) was larger for the homogeneous fault than for the heterogeneous faults. For the homogeneous gypsum fault slip events propagated over the entire fault (Fig. 3a). A local stress drop of 0.4–0.5 MPa (consistent with τ^* in Fig. 2a) was observed at all strain traces. The shear displacement rate obtained from the 1 fps image data also indicates that the entire fault slipped during the slip event (Fig. 3a). For the heterogeneous fault compositions on the other hand slip only extended over part of the fault – i.e. confined rupture events. The smallest events occurred for the calcite-gypsum fault (Fig. 3c, Fig. 4a). The stress drop (~ 0.05 MPa) between SG122 and SG220 indicated that the slip events had a length of ~ 100 mm. Further away from the gypsum segment the shear stress increased after the event, indicating arrest of the slip event and stress transfer to adjacent regions (Fig. 3c, Fig. 4a). The partial slip events were also visible in the image data, where elevated shear displacement rates are seen along the gypsum segment, but can barely be discerned outside of the gypsum segment (Fig. 3c). Larger events occurred on the quartz-gypsum fault, with a rupture length of ~ 120 – 140 mm between SG108 and SG220–248 (Fig. 4b, Fig. 5a). The stress drops observed on the gypsum segment were also larger than for the events on the calcite-gypsum fault, with an average stress drop of 0.12 MPa (Fig. 5a). The rupture length was largest for the kaolinite-gypsum fault, where almost the entire fault slipped during the stick-slip event (Fig. 4c). Slip was still strongly concentrated within the gypsum segment though, which experienced an average stress drop of 0.1–0.15 MPa (Fig. 5b). The smaller macroscopic stress drops for the heterogeneous faults (Fig. 2) are thus reflected in smaller local stress drops and rupture size.

Correspondingly, the shear displacements and slip rates were largest for slip events on the homogeneous gypsum fault and decreased for the heterogeneous faults. The total fault-averaged shear displacement attained over the slip event in Fig. 3a was 103 μm . High framerate image data revealed maximum slip rates of 0.2 ms^{-1} (Buijze et al., 2020). This slip rate is well above the dynamic slip rate V_{dyn} , which is the slip rate above which inertial effects start to play a role (Rubin and Ampuero, 2005). $V_{dyn} = \sigma_n^* a V_s / G$ where a is the rate-and-state parameter and V_s is the S-wave velocity ($= 1350 \text{ ms}^{-1}$ for PMMA) and G is the shear modulus (1.1 GPa for PMMA); for a normal stress of 10 MPa and $a = 0.003$

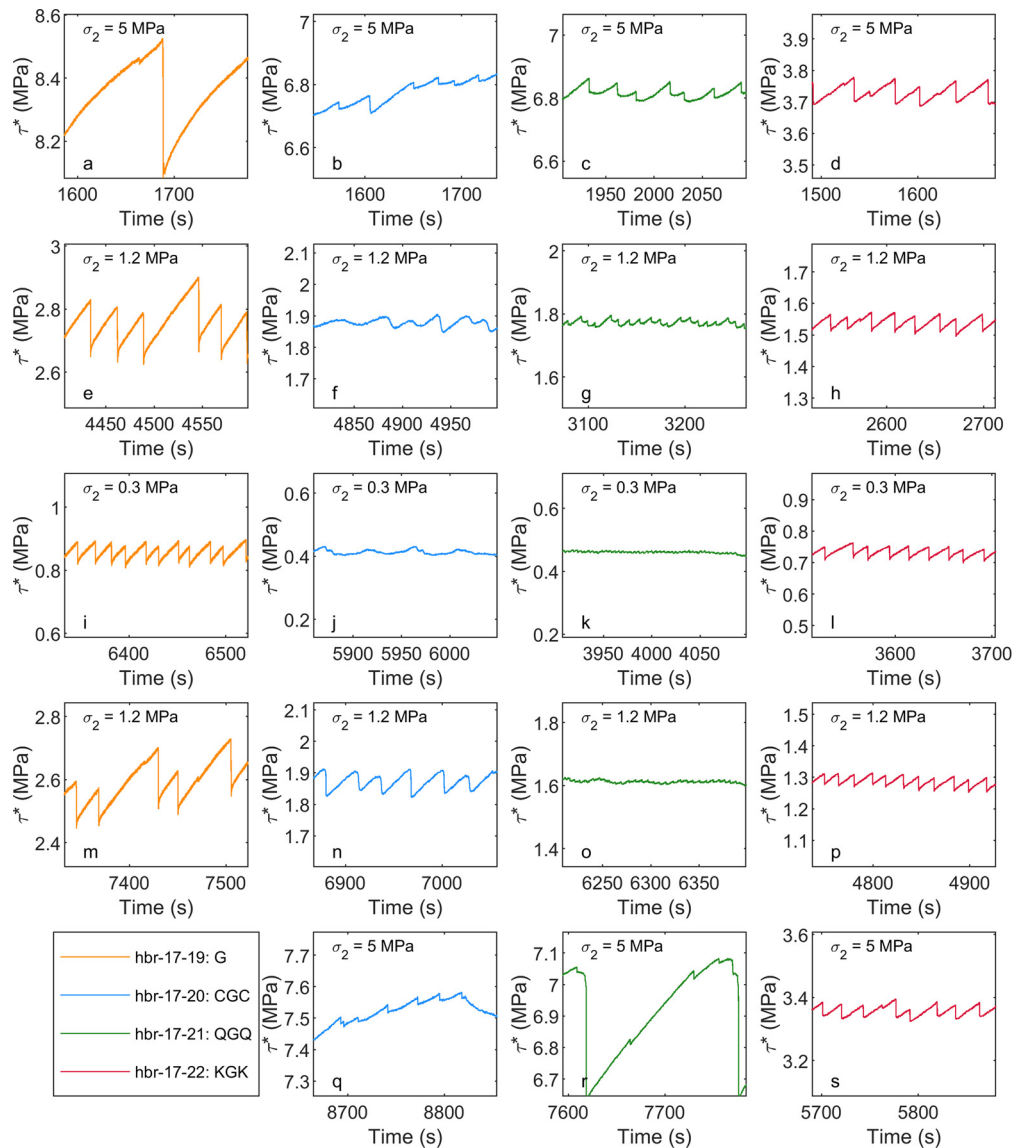


Fig. 2. Mechanical data showing stick-slips and macroscopic fault shear stress for different fault lithologies at 5, 1.2, and 0.3 MPa confining stress σ_2 . a, e, i, m) homogeneous gypsum fault (G), b, f, j, n, q) calcite-gypsum fault (CGC), c, g, k, o, r) quartz-gypsum fault (QGQ), d, h, l, p, s) kaolinite-gypsum fault (KGK). The applied σ_2 is indicated at the top of each subplot.

the V_{dyn} is 0.035 ms^{-1} (Fig. 6f). Displacement and slip rates are significantly lower along the gypsum segment on the heterogeneous faults. The total displacement attained on the gypsum segment of the calcite-gypsum fault was $10\text{--}15 \text{ }\mu\text{m}$ (Fig. 3d). Unfortunately no high framerate data was available for these events so slip rate could not be determined. For the quartz-gypsum fault the average shear displacement attained during the events on the gypsum segment was larger ($d_{tVW} = 15\text{--}20 \text{ }\mu\text{m}$) (Fig. 3f, Fig. 4b, Fig. 5a and g). Here the average maximum slip rate in the gypsum segment was 0.011 ms^{-1} , which is an order of magnitude lower than the slip rates on the homogeneous gypsum fault and $\sim 30\%$ of V_{dyn} . Shear displacement and slip rates were larger for the kaolinite-gypsum fault, with an average slip of $25 \text{ }\mu\text{m}$ in the gypsum segment and an average maximum slip rate of 0.015 ms^{-1} , 45% of the dynamic value (Fig. 6d). The kaolinite segments slipped with $10 \text{ }\mu\text{m}$, but slip rates were lower than in the gypsum with an average slip rate of $0.005\text{--}0.01 \text{ ms}^{-1}$.

In all cases, (significant) precursory slip occurred on the gypsum fault or gypsum fault segments during the entire interseismic period (i.e. the time between slip events). The contribution of precursory slip was smallest for the homogeneous gypsum fault. Shear

displacement rates during the interseismic period fall below the noise level of the image data (Fig. 3a), but a cumulative shear displacement of $18 \text{ }\mu\text{m}$ was observed prior to the slip event (Fig. 3b). The cumulative shear displacement includes elastic deformation in the 20 mm of PMMA across which the shear displacement is calculated (see Methods), which is $\sim 10 \text{ }\mu\text{m}$ for the stress buildup of 0.5 MPa in the interseismic period. This implies that $8 \text{ }\mu\text{m}$ of precursory slip occurred, which is 10% of the slip in the subsequent slip event. For the heterogeneous faults the precursory slip contribution is larger. For the calcite-gypsum fault the calcite segments slipped at approximately the applied far-field displacement rate (Fig. 3d). Meanwhile $18 \text{ }\mu\text{m}$ of precursory fault slip occurred on the gypsum segment in the interseismic period, which is comparable to the shear displacement during the slip event itself. Similar amounts of precursory slip were recorded on the gypsum segment for the quartz-gypsum fault (Fig. 3f, Fig. 5g) and the kaolinite-gypsum fault. Less precursory slip was recorded on the gypsum segment for the kaolinite-gypsum fault (Figure). Here, slip in the interseismic period was $10 \text{ }\mu\text{m}$, which is 30% of the shear displacement of the subsequent slip event. Precursory slip occurring at the edges of the VW segment just prior to the slip event can also be

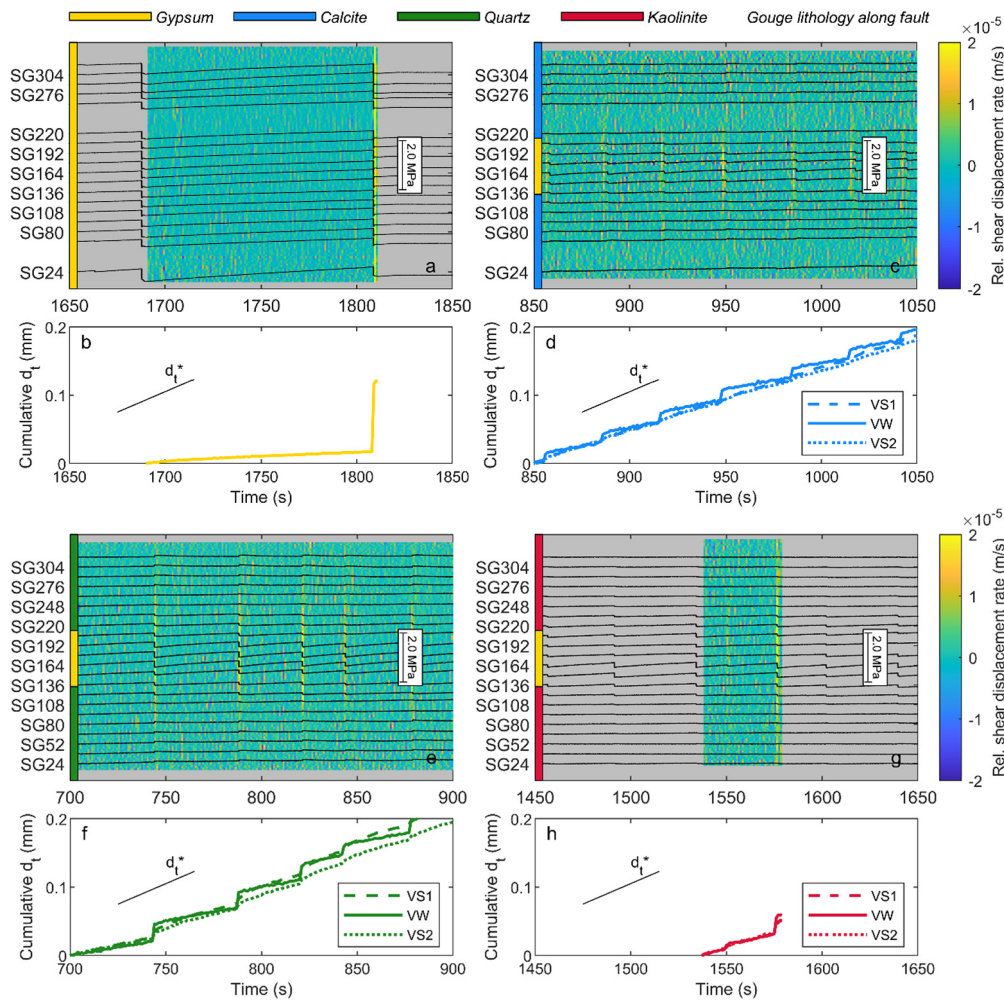


Fig. 3. Shear stresses and displacements along the fault margin during shearing ($\sigma_2 = 5$ MPa). For a, c, e, and g, stress traces at different locations along the fault are shown as a function of time from the start of shearing. Background colors show the relative shear displacement rate across the fault obtained from DIC of the 1 fps image data; for the grey areas no image data was available. The background is colored grey where no image data was available. a) Gypsum fault, c) calcite-gypsum fault, e) quartz-gypsum fault, g) kaolinite-gypsum fault. Subplots b, d, f, and h show the cumulative displacements along the fault averaged over the VS segments and the VW segment, corresponding to the time series shown in respectively a, c, e, and g. The imposed macroscopic displacement is also indicated (d_t^*)

observed in Fig. 4c, which is also reflected by slow yielding in the strain signals prior to the event.

To summarize, at $\sigma_2 = 5$ MPa slip events on the heterogeneous faults originated in the VW segment and were arrested in the VS segments, and thus had smaller rupture length, less slip and lower slip rates, and more precursory slip in the interseismic phase compared to the homogeneous gypsum fault.

3.3. Slip behavior at lower σ_2

For the gypsum fault slip events persisted upon lowering σ_2 , but a larger part of the fault was yielding and slipping slowly prior to the slip events (Buijze et al., 2020). Concurrently the displacement and maximum slip rates decreased, from 105 μm and 0.2 ms^{-1} ($\sigma_2 = 5$ MPa, or $\sigma_n = 10.5$ MPa) to 20 μm and 0.01 ms^{-1} ($\sigma_2 = 0.3$ MPa, or $\sigma_n = 1$ MPa) (Fig. 6 e, f).

The sliding characteristics of the three heterogeneous fault compositions showed marked differences upon lowering σ_2 . Periodic slow-slip events were observed for the calcite-gypsum fault, where the fault slipped uniformly over its entire length (Fig. 4d, Fig. 5i). The stress drop was 0.1 MPa, but the duration of the events increased from 3 ms at $\sigma_2 = 5$ MPa to over 10–20 s at $\sigma_2 = 0.3$ MPa (Fig. 5c, i, Fig. 6b, c). The cumulative slip attained during the events was 30–40 μm , at a maximum slip rate of sev-

eral μms^{-1} , just above the applied load point velocity. For the quartz-gypsum fault stable sliding was observed after lowering the σ_2 to 0.3 MPa, but small stick-slips appeared after 0.2 mm of sliding under these conditions (Fig. 4e). Small stress drops of 0.01 MPa were observed in the gypsum segment, but the duration (several ms to 0.01 s) indicated that the events were significantly slower than those at higher σ_2 (Fig. 6b). For the kaolinite-gypsum fault stick-slip behavior persisted down to 0.3 MPa. The stress drop on the gypsum segment was 0.05 MPa, which is three times smaller than at $\sigma_2 = 5$ MPa (Fig. 6a). The average slip on the gypsum patch was 15 μm , but slip rates were similar to those at higher σ_2 (Fig. 4f, Fig. 6e, f).

3.4. Fault normal deformation

The different gouges along the fault do not only have different strengths and velocity-dependences, but also compact differently in response to the applied normal and shear loads, which can lead to heterogeneous fault normal stresses (Buijze et al., 2020). Fault-normal deformation (compaction) obtained from DIC shows a large difference between kaolinite and gypsum compaction (Fig. 7a). Prior to shearing, compaction along the kaolinite segments amounted to 0.6–0.8 mm, whereas compaction along the gypsum segment was 0.2 mm (Fig. 7b). For the other fault compo-

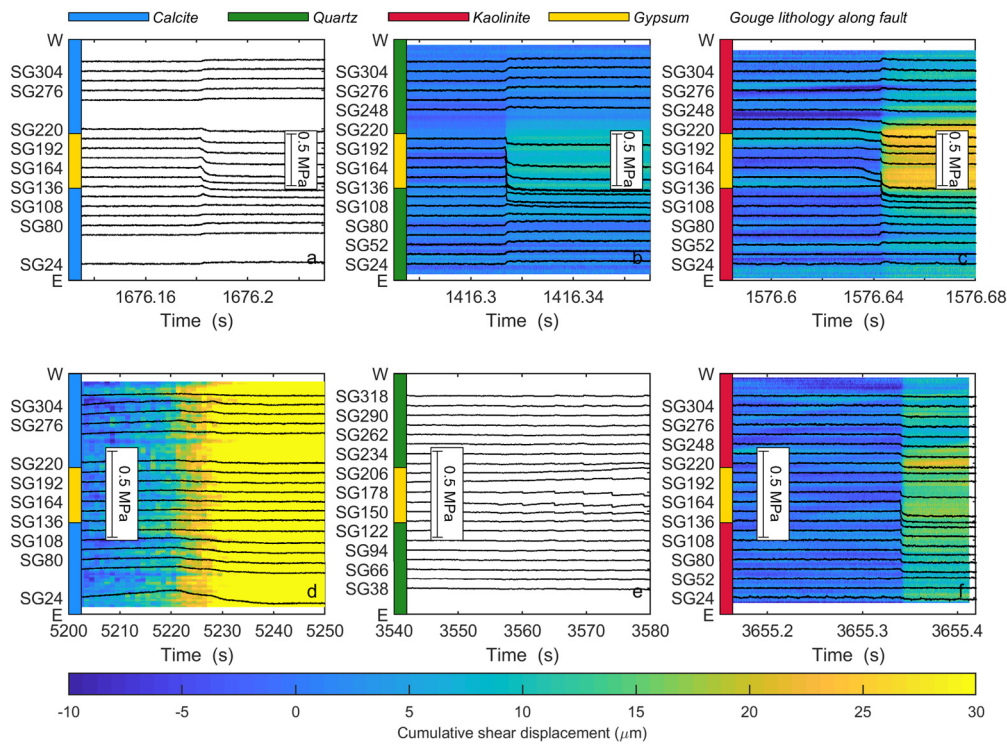


Fig. 4. Zoom-in of selected slip events for the heterogeneous faults at different confining stresses. Background colors depict the cumulative shear displacements across the fault obtained from DIC; white colors indicate no DIC was available, e.g. in a and e or near the fault ends. For b, c, and f high resolution image data was used (5000–9000 fps), for d the 1 fps data was used. a) Calcite–gypsum fault at 5 MPa, b) quartz–gypsum fault at 5 MPa, c) kaolinite–gypsum at 5 MPa, d) calcite–gypsum at $\sigma_2 = 0.3$ MPa, e) quartz–gypsum at $\sigma_2 = 0.3$ MPa, f) kaolinite–gypsum at $\sigma_2 = 0.3$ MPa.

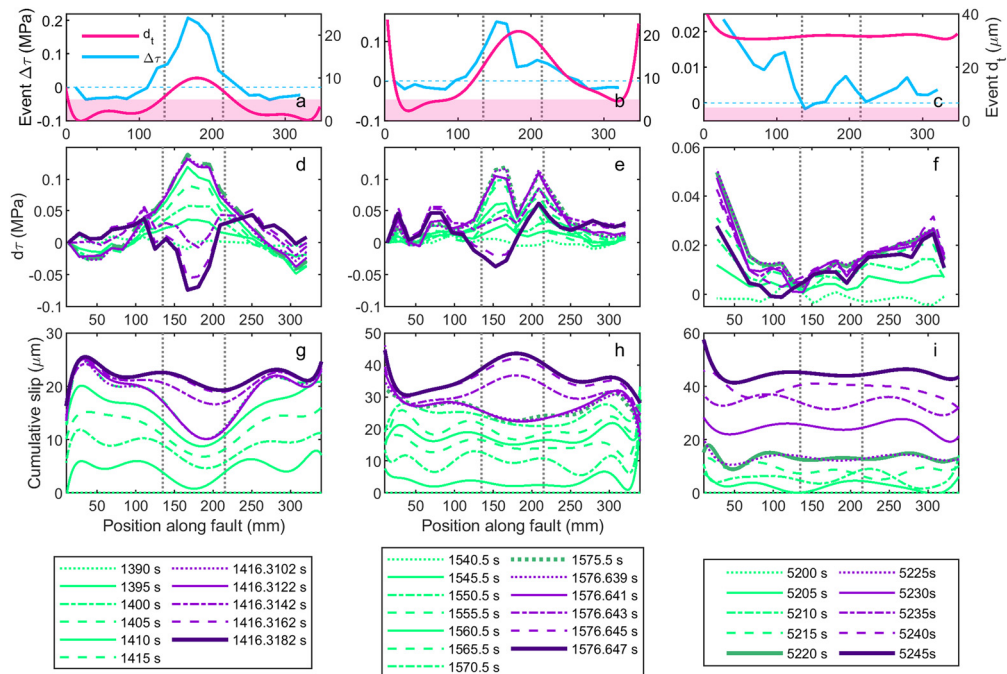


Fig. 5. Distribution of shear stress and slip along the fault at different points in time. Slip events are shown for a, d, g) the quartz–gypsum fault at $\sigma_2 = 5$ MPa, b, e, h) the kaolinite–gypsum fault at $\sigma_2 = 5$ MPa, c, f, i) the calcite–gypsum fault at $\sigma_2 = 0.3$ MPa. The position of the VW gypsum segment is indicated by the dotted lines. The slip distribution obtained from DIC is shown in g–i, with time snapshots during the loading phase prior to the slip event indicated by the green lines (timestep = 5 s), and purple line indicating the slip evolution during the slip event (timestep = 0.002 s, or for calcite–gypsum, 5 s). The coseismic cumulative slip (pink) and the stress drop $\Delta\tau$ (blue) (i.e. difference in shear stress before w.r.t. after the slip event, positive is stress drop, negative is stress increase) for the three fault compositions is shown in a–c. The pink shaded area indicates the resolution of the DIC measurements.

sitions the difference in compaction between the VS segments and the gypsum segment (~ 0.1 to 0.2 mm) was smaller as compaction of the VS segments (calcite, quartz) was less than that of kaolinite. The difference in compaction decreased as shear displacement

along the fault increased, as the gypsum segment compacted more during shearing (Fig. 7c). For calcite–gypsum and quartz–gypsum the compaction of the VS and VW segments was almost equal at $\sigma_2 = 0.3$ MPa. For kaolinite–gypsum the compaction difference be-

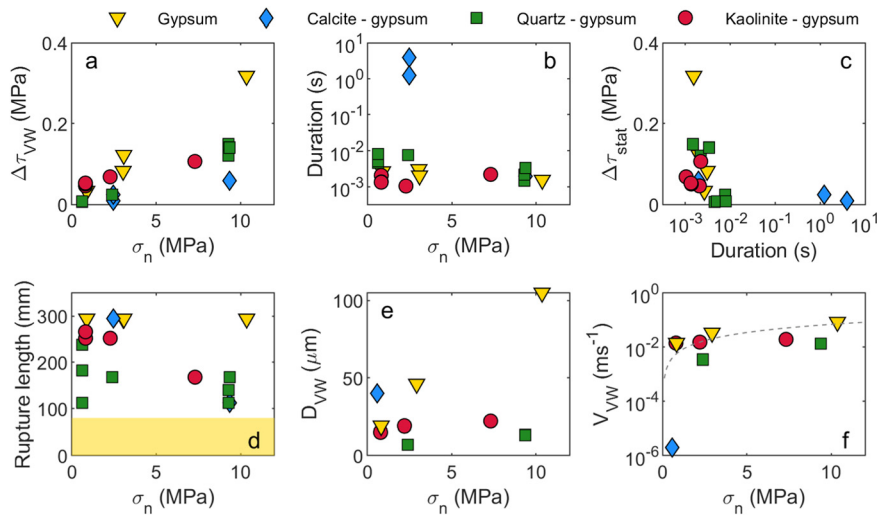


Fig. 6. Metrics of selected stick-slip events determined from the strain gauge data (a–d) and DIC data (e–f). Blue diamond: calcite-gypsum fault, green squares: quartz-calcite fault, red circles: kaolinite-gypsum fault. a) Confining stress σ_2 against average stress drop in the VW segment, b) σ_2 against duration of the event, c) duration against average static stress drop in the gypsum segment, d) σ_2 against rupture length, with the yellow area indicating the initial length of the gypsum segment, e) σ_2 against average displacement on the gypsum segment, f) σ_2 against maximum slip rate on the gypsum segment. The line in f shows the dynamic slip rate V_{dyn} which is given as $V_{dyn} = \sigma_n a V_s / G$ (Rubin and Ampuero, 2005) above which inertial effects start to play a role. Note that V_{dyn} was computed using the fault-average macroscopic stress.

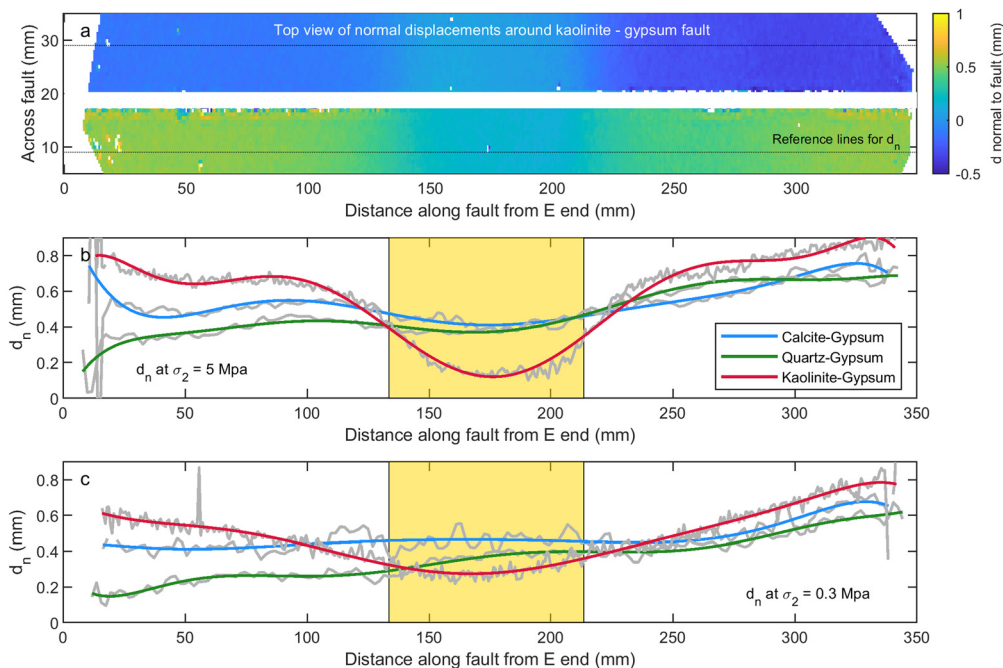


Fig. 7. Fault-normal deformation from image analysis. a) Fault-normal displacements in the area around the fault imaged by the camera. Positive indicates motion southwards, negative northwards. b) Relative fault normal displacement d_n along the fault after 3.5 mm sliding at $\sigma_2 = 5$ MPa. c) Relative fault normal displacement d_n after 5–7 mm of sliding and at $\sigma_2 = 0.3$ MPa. In b and c the initial position of the gypsum segment is indicated. Grey lines indicate raw data, colored line an 8th order polynomial fit through the displacement data.

tween the segments decreased significantly and d_n along the fault became smoother.

The largest normal stress differences are thus expected for the kaolinite-gypsum fault, with normal stress concentrated on the gypsum segment which compacts significantly less than the kaolinite segments. With shear displacement the normal stress differences are expected to decrease as the gouge compaction differences become less.

4. Discussion

Frictional heterogeneity on the experimental faults led to different slip behaviors depending on the confining stresses and/or

lithology, including partial or confined ruptures, full-fault slow slip events, and near-stable sliding. The effect of frictional heterogeneity on slip behavior has also been analyzed in theoretical and numerical modeling studies. Partial ruptures, or P-instabilities, as well as full-fault ruptures (T-instabilities), slow slip events, and stable sliding were also observed in a numerical modeling study of a single-asperity fault with a VW segment flanked by VS segments (Luo and Ampuero, 2018) similar to the experimental setup. The authors found that the slip behavior depended on the critical nucleation length $L_c = \frac{GD_c}{(b_{VW} - a_{VW})\sigma_{nVW}}$ with respect to the length of the VW segment L_{VW} ($\beta = L_{VW}/L_c$), the relative strength α which is the ratio between the amount of weakening in the VW

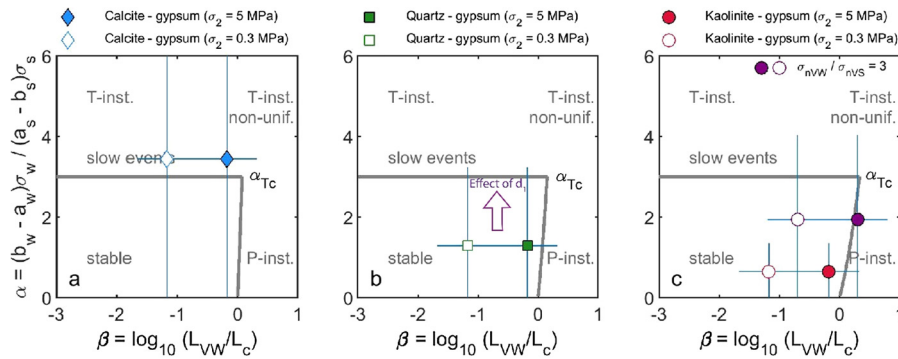


Fig. 8. Position of heterogeneous experimental fault compositions in stability diagram derived from linear stability analysis of a single asperity VW segment within VS material. Stability boundaries (grey lines) are plotted using Eq. (54) and Eq. (33) (α_{TC}) in Luo and Ampuero, 2018 (W assumed large due to free upper and lower fault margin), and associated slip behavior is indicated by the grey text, where T-inst.: total instability rupturing the entire fault, P-inst.: partial instability rupturing the VW segment, but arresting in the VS segment, non-unif.: T-instability but with non-uniform fault slip being largest in the VW segment. The average RSF parameters from Table 1 and the associated uncertainty were used to plot a) the calcite-gypsum fault, b) the quartz-gypsum fault, and c) the kaolinite-gypsum fault. Closed symbols: $\sigma_2 = 5$ MPa, open symbols: $\sigma_2 = 0.3$ MPa.

segment to the amount of strengthening of the VS segments $\alpha = \frac{(b_{vw} - a_{vw})\sigma_{vw}}{(a_{vs} - b_{vs})\sigma_{vvs}}$, as well as the ratio of VW to VS material $VW:VS$. The boundaries between the different slip regimes could be derived from linear stability analysis (Luo and Ampuero, 2018); in Fig. 8 these boundaries are redrawn for our experimental setup. The near-vertical boundary is close to $\beta = 1$ and separates P-instabilities from stable sliding, and the horizontal boundary α_{TC} (here ~ 3) separates stable sliding and T-instabilities. To compare the experimentally observed slip behaviors to the theory, the position of the experimental faults is also plotted in Fig. 8, with L_c obtained from the mean RSF parameters of gypsum, and relative strength α from the mean RSF values of gypsum and the VS lithology (Table 1, Fig. S2). At the highest confining stress $L_c = 0.11$ m, slightly larger than the length of the VW segment ($\beta \sim 1$). For the quartz-gypsum and kaolinite-gypsum fault $\alpha < 3$, which places these compositions close to the P-instability boundary (Fig. 8b and c), consistent with the observed partial ruptures on these experimental faults. Note that the uncertainty in RSF parameters is significant, and the sharp boundaries indicated in Fig. 8 derives from uniform slip assumptions on the VW patch; heterogeneous stresses and slip on the VW segment as expected in the experiment can result in a broader transition regime between unstable and stable sliding (Luo and Ampuero, 2018; Skarbek et al., 2012) so that instability could occur even if β is slightly larger than 1. The proximity to the stability boundary is also manifest by the significant precursory slip observed on the VW segment (Chen and Lapusta, 2009), as well as the relatively low slip rates during the slip event.

At lower σ_n of 1 MPa ($\sigma_2 = 0.3$ MPa) the stability of the experimental faults shifts to the left, into the stable sliding regime. Indeed for the quartz-gypsum stable sliding occurred after lowering the confining stress to 0.3 MPa, but small stick-slips reappeared after ~ 0.3 mm of load point-displacement, rupturing the edge of the VW patch. Shear stress was elevated on the (edges of the) VW patch (Fig. S6) as it is loaded by stable sliding on the VS segments. This may cause the nucleation length to shrink (e.g. Guérin-Marthe et al., 2019) and may promote the persistence of small stick-slip events even though $L_c > L_{VW}$. Instability can also develop as the slip zones from the edges of the VW segments coalesce. Stick-slip behavior persisted for the kaolinite-gypsum fault at low normal stresses, even though stable sliding is expected from the theory. Stronger shear and normal stress concentrations are present in this experiment, as respectively the frictional strength of the segments differs significantly (0.3 vs 0.8), and the compaction within the VS segments is much larger than within the VW which will lead to an elevated σ_{nVW} (Fig. S6, see also Buijze et al., 2020). The concentrated normal stress places the fault

in a more unstable regime, with a smaller L_{VW}/L_c and a higher α (example shown for $\sigma_{nVW}/\sigma_{nVS} = 3$ in Fig. 8c), which may explain the persistence of stick-slip behavior towards lower normal stresses, in addition to the points mentioned above. For the calcite-gypsum fault at $\sigma_2 = 5$ MPa $\beta \sim 1$ but the relative strength exceeds α_{TC} which places its expected behavior in the T-instability field (Fig. 8c). However, at the highest normal stress partial rupture were observed in the experiments. Note that uncertainties in α are substantial due to the scatter in the RSF data. Also, $a - b$ of calcite increases with increasing normal stress (Carpenter et al., 2016, Fig. S2), so the α computed from the mean values may overestimate the actual relative strength at $\sigma_2 = 5$ MPa. Lowering the stress on the calcite-gypsum fault resulted in periodic slow slip events with a period of ~ 40 s and a slip rate of several $\mu\text{m/s}$. Numerical modeling showed that slow slip earthquakes occur near the stability boundary defined by α_{TC} (Luo and Ampuero, 2018), which is consistent with the experimental observations. The period of slow slips may have been modulated by the loading stresses; small (± 3 kPa) oscillations of 35–45 s were observed in the applied σ_2 . VW materials near the stability boundary or materials near velocity neutral may be sensitive to small periodic loads (Perfettini and Ampuero, 2008). Resonant slow events are for example also proposed for SSE in subduction zones subject to a small seasonal stress changes (Lowry, 2006).

In general, the observed slip behaviors are consistent with previous theoretical and modeling studies on heterogeneous faults. However, discrepancies between the expected and observed behavior can occur because of heterogeneous fault stresses, uncertainties in the RSF data, and evolution of the RSF parameters with normal stress and/or displacement. Though for gypsum, kaolinite, and calcite the effect of displacement appears limited, for quartz a clear decrease in $a - b$ is observed from positive values at displacements < 10 mm to negative values at larger displacements (Fig. S2). This progressive decrease of $a - b$ of quartz is reflected by the slip behaviors of the heterogeneous quartz-gypsum fault at larger displacements, after stepping up the confining stress back to 1.2 and 5 MPa. During the second slip stage at 1.2 MPa, long-period oscillations superimposed with small stick-slips were observed (Fig. 2m), in contrast to the larger slip events seen during the first slip stage at 1.2 MPa (Fig. 2k). This is consistent with an increase of α resulting from the decrease of $a - b$, which would move the stability of the quartz-gypsum fault towards the α_{TC} boundary (Fig. 8b). At the second slip stage at $\sigma_2 = 5$ MPa (d_1 10–11 mm) large stick-slip cycles occur with stress drops comparable to those observed on the homogeneous gypsum fault, superimposed with smaller slip events with smaller recurrence times (Fig. 2n). The strain data (not

shown here) show that the smaller events are related to rupture of the gypsum segments, and the larger events are related to slip of the entire fault – i.e. super-cycle behavior. The period of the smaller slip events decreases throughout the slip cycle (Fig. 2n), which is also seen in modeled super-cycles at high α (Luo and Ampuero, 2018), as well as in modeling of slow-slip events at the base of the seismogenic zone (Luo and Liu, 2019b), and could also be recognized on natural faults. It will be worthwhile for future experimental studies to investigate the slip behavior on heterogeneous faults with large α or spatially varying VW properties, in addition to the combination of VS and VW segments used here.

To summarize, the observed slip behaviors are consistent with RSF theory and numerical modeling of frictionally heterogeneous faults, but the transition regimes may be broader due to non-uniform slip on the VW segment. Also shear and normal stress concentrations play an important role. Stress concentrations could result in more unstable fault than expected from the far-field stresses. Numerical modeling of a VW fault with multiple asperities carrying a high normal load also shows how many small foreshock result from loading by aseismic slip of the surrounding fault region (Schaal and Lapusta, 2019). This suggests stress concentrations on natural faults could cause small, relatively slow instabilities to occur even on asperities smaller than the critical nucleation length, as seen on the kaolinite- or quartz-gypsum fault. When the VW asperity is larger rupture can propagate further into the VS region; the experiments showed rupture length varied depending on the properties of the VS material. Similarly, rupture may nucleate on VW patches on natural faults (e.g. brittle lenses, particular stratigraphic intervals) and propagate into VS regions. Note also that even on a fully VW fault, both partial, slower ruptures and faster ruptures can occur depending on the length-scale of the stress concentration and the critical nucleation length, as demonstrated experimentally by Wu and McLaskey (2019). To assess how far ruptures could propagate on natural faults it is important to know the both the stresses and in-situ RSF parameters for the different fault regions, as shown for example for the Lorca fault where rupture may have nucleated in highly stressed competent fault lenses but propagated into the shallow VS region (Niemeijer and Vissers, 2014).

In case of induced seismicity, the local state of stress may be severely altered due to operations such as fluid injection or hydrocarbon depletion. In the vast seismogenic Groningen gas field in the northeast Netherlands, for example, reservoir depletion will cause an ongoing increase in shear and normal stress on the fault section in and near the reservoir interval leading to rupture nucleation (e.g. Buijze et al., 2019). Gas production in the Netherlands (and other anthropogenic activities in the subsurface) involves layered sedimentary system, for which frictional properties are expected to vary significantly along the faults. Friction measurements on gouges from typical lithologies in the Groningen field showed significant variability in RSF properties of the reservoir and over- and underburden lithologies (Hunfeld et al., 2017). Current numerical models of (depletion-)induced seismicity have not extensively evaluated the sensitivity of rupture size to these variations in frictional strength and stability, although variable friction was incorporated in Buijze et al. (2017), and variations of frictional strength have been incorporated statistically in seismological models of the Groningen field (Bourne et al., 2018). Also a distribution of VW and VS asperities was prescribed on a fault subjected to pressure diffusion due to waste water injection shows which influences the seismicity rate and b-value (Almakari et al., 2019). We recommend to investigate the effect of frictional heterogeneity on fault slip behavior and event magnitude for future modeling studies of induced seismicity. In particular we recommend to investigate the relation between the length-scale of the frictional heterogeneity (e.g. the sedimentary layering), the length-scale of the induced stress per-

turbation, and the typical nucleation length-scales of the faulting process. If these length-scales are of the same order, frictional variability may have a large effect on the earthquake dynamics (Ray and Viesca, 2017), as was also observed in our study. Incorporation of frictional heterogeneity, as well as stress variations along fault subjected to anthropogenic loading will lead to improved understanding of the slip behavior as well as potential rupture sizes, and the potential for rupture to propagate outside its nucleation area into other fault lithologies.

5. Conclusions

We investigated experimentally the sliding characteristics of three 350 mm long frictionally heterogeneous faults and one homogeneous fault sandwiched by PMMA blocks. The fault lithology was controlled by gouge and consisted of a 80 mm long central velocity-weakening (VW) segment, flanked by two velocity-strengthening (VS) segments. The VW segment was composed of gypsum gouge, and the VS segments were composed of either calcite, quartz, or kaolinite gouge. The confining stress σ_2 was stepped during the experiments from 5 to 0.3 MPa, corresponding to an order of magnitude difference in macroscopic normal stress (10.5 to 1 MPa). Here we summarize the main findings:

- unstable sliding was observed for all three heterogeneous fault compositions at nearly all the experimental conditions evaluated.
- at $\sigma_2 = 5$ MPa partial ruptures occurred which predominantly ruptured the VW gypsum segment, and propagated to certain extent into the VS segment. The smallest ruptures were observed for calcite-gypsum, the largest for kaolinite-gypsum. The corresponding stress drops of 0.02 to 0.1 MPa, were more than 5 times smaller than the stress drops observed on the homogeneous gypsum fault which ruptured over its entire length. Slip rates on the VW segment were on the order of 0.01 ms^{-1} .
- significant precursory slip occurred on the VW segment during the interseismic period, amounting up to 50% of the total slip.
- towards lower σ_2 the sliding behavior differed per fault composition:
 - for calcite-gypsum, a transition to slow slip events with a duration of 10–20 s was observed,
 - for quartz-gypsum, a transition to near-stable sliding was observed,
 - for kaolinite-gypsum, stick-slips persisted.
- however, the heterogeneous state of stress on the fault also plays a role.
 - shear stress concentrations form at the edges of the VW segment, promoting occurrence of small, slow slip events,
 - normal stress concentrated on the VW segment due to differences in gouge compaction. This effect was strongest for kaolinite-gypsum, causing the fault to remain unstable even at low σ_2 .
- these sliding characteristics are generally consistent with numerical models of frictionally heterogeneous faults governed by rate-and-state friction. The results show that including frictional heterogeneity, on top of stress heterogeneity, is important for understanding sliding behavior of faults subjected to tectonic and/or anthropogenic stressing.

CRediT authorship contribution statement

L. Buijze: Conceptualization, Investigation, Methodology, Visualization, Writing – original draft, Writing – review & editing. **Y. Guo:** Data curation, Investigation, Methodology, Resources, Writing

– review & editing. **A.R. Niemeijer:** Conceptualization, Funding acquisition, Supervision, Writing – review & editing. **S. Ma:** Funding acquisition, Project administration, Resources, Writing – review & editing. **C.J. Spiers:** Conceptualization, Funding acquisition, Project administration, Supervision, Writing – review & editing.

Declaration of competing interest

The authors declare that they have no known competing financial interests or personal relationships that could have appeared to influence the work reported in this paper.

Acknowledgements

This study was performed in the context of the research program “Studies on fault (re)activation and dynamic friction and failure behavior” (Research Agreement UI49294) funded by the Nederlandse Aardolie Maatschappij (NAM). This program focuses on a fundamental understanding of the physical mechanisms of production-induced reservoir compaction and induced seismicity in the Groningen gas field. André Niemeijer is supported by the European Research Council, starting grant SEISMIC (335915) and by the Dutch Research Council (NWO) Vidi-grant 854.12.001. This work was also partly supported by the National Natural Science Foundation of China (grant number U1839211). CEA employees Yuntao Ji, Wenbo Qi and Yan-Qun Zhuo, and UU employees Thony van der Gon-Netscher and Floris van Oort are thanked in particular for technical assistance in the laboratories at CEA and UU. Furthermore the authors would like to thank Dirk Doornhof for his feedback and Pablo Ampuero for discussions on fault stability. We thank Vincent Brunst for his help with data publication; mechanical data, selected strain data and image data are available in the Yoda repository of UU (<https://doi.org/10.24416/UU01-2RECP2>).

Appendix A. Supplementary material

Supplementary material related to this article can be found online at <https://doi.org/10.1016/j.epsl.2020.116652>.

References

- Almakari, M., Dublanchet, P., Chauris, H., Pellet, F., 2019. Effect of the injection scenario on the rate and magnitude content of injection-induced seismicity: case of a heterogeneous fault. *J. Geophys. Res., Solid Earth* 124 (8), 8426–8448.
- Ariyoshi, K., Hori, T., Ampuero, J., Kaneda, Y., Matsuzawa, T., Hino, R., Hasegawa, A., 2009. Influence of interaction between small asperities on various types of slow earthquakes in a 3-D simulation for a subduction plate boundary. *Gondwana Res.* 16 (3–4), 534–544.
- Barbot, S., 2019. Slow-slip, slow earthquakes, period-two cycles, full and partial ruptures, and deterministic chaos in a single asperity fault. *Tectonophysics* 768, 228171.
- Bourne, S.J., Oates, S.J., van Elk, J., 2018. The exponential rise of induced seismicity with increasing stress levels in the Groningen gas field and its implications for controlling seismic risk. *Geophys. J. Int.* 213 (3), 1693–1700.
- Buijze, L., Guo, Y., Niemeijer, A.R., Ma, S., Spiers, C.J., 2020. Nucleation of stick-slip instability within a large-scale experimental fault: effects of stress heterogeneities due to loading and gouge layer compaction. *J. Geophys. Res., Solid Earth* 125 (8), e2019JB018429.
- Buijze, L., van den Bogert, P., Wassing, B.B.T., Orlic, B., 2019. Nucleation and arrest of dynamic rupture induced by reservoir depletion. *J. Geophys. Res., Solid Earth* 124 (4), 3620–3645.
- Buijze, L., van den Bogert, P.A.J., Wassing, B.B.T., Orlic, B., ten Veen, J., 2017. Fault reactivation mechanisms and dynamic rupture modelling of depletion-induced seismic events in a Rotliegend gas reservoir. *Neth. J. Geosci.* 96 (5), s131–s148.
- Carpenter, B.M., Collettini, C., Viti, C., Cavallo, A., 2016. The influence of normal stress and sliding velocity on the frictional behaviour of calcite at room temperature: insights from laboratory experiments and microstructural observations. *Geophys. J. Int.* 205 (1), 548–561.
- Chen, T., Lapusta, N., 2009. Scaling of small repeating earthquakes explained by interaction of seismic and aseismic slip in a rate and state fault model. *J. Geophys. Res.* 114 (B01311).

- Collettini, C., Niemeijer, A., Viti, C., Smith, S.A., Marone, C., 2011. Fault structure, frictional properties and mixed-mode fault slip behavior. *Earth Planet. Sci. Lett.* 311 (3–4), 316–327.
- Das, I., Zoback, M., 2013. Long-period, long-duration seismic events during hydraulic stimulation of shale and tight-gas reservoirs – Part 1: waveform characteristics. *Geophysics* 78 (6), KS97–KS108.
- de Meer, S., Spiers, C.J., 1997. Uniaxial compaction creep of wet gypsum aggregates. *J. Geophys. Res., Solid Earth* 102 (B1), 875–891.
- Derode, B., Guglielmi, Y., De Barros, L., Cappa, F., 2015. Seismic responses to fluid pressure perturbations in a slipping fault. *Geophys. Res. Lett.* 42 (9), 3197–3203.
- Fagereng, Å, Sibson, R.H., 2010. Melange rheology and seismic style. *Geology* 38 (8), 751–754.
- Faulkner, D., Lewis, A., Rutter, E., 2003. On the internal structure and mechanics of large strike-slip fault zones: field observations of the Carboneras fault in south-eastern Spain. *Tectonophysics* 367 (3–4), 235–251.
- Guérin-Marthe, S., Nielsen, S., Bird, R., Giani, S., Di Toro, G., 2019. Earthquake nucleation size: evidence of loading rate dependence in laboratory faults. *J. Geophys. Res., Solid Earth* 124 (1), 689–708.
- Hunfeld, L.B., Niemeijer, A.R., Spiers, C.J., 2017. Frictional properties of simulated fault gouges from the seismogenic Groningen gas field under in situ P-T – chemical conditions. *J. Geophys. Res., Solid Earth* 122 (11), 8969–8989.
- Ikari, M.J., Carpenter, B.M., Marone, C., 2016. A microphysical interpretation of rate- and state-dependent friction for fault gouge. *Geochem. Geophys. Geosyst.* 17 (5), 1660–1677.
- Ito, Y., Obara, K., Shiomi, K., Sekine, S., Hirose, H., 2007. Slow earthquakes coincident with episodic tremors and slow slip events. *Science* 315 (5811), 503–506.
- Kumar, A., Zorn, E., Hammack, R., Harbert, W., 2019. Long-period, long-duration seismic events and their probable role in reservoir stimulation and stage productivity. *SPE Reserv. Eval. Eng.* 22 (02), 441–457.
- Leeman, J., Saffer, D., Scuderi, M., Marone, C., 2016. Laboratory observations of slow earthquakes and the spectrum of tectonic fault slip modes. *Nat. Commun.* 7, 11104.
- Linde, A.T., Gladwin, M.T., Johnston, M.J., Gwyther, R.L., Bilham, R.G., 1996. A slow earthquake sequence on the San Andreas fault. *Nature* 383 (6595), 65.
- Lowry, A.R., 2006. Resonant slow fault slip in subduction zones forced by climatic load stress. *Nature* 442 (7104), 802.
- Luo, Y., Ampuero, J., 2018. Stability of faults with heterogeneous friction properties and effective normal stress. *Tectonophysics* 733, 257–272.
- Luo, Y., Liu, Z., 2019a. Rate-and-state model casts new insight into episodic tremor and slow-slip variability in Cascadia. *Geophys. Res. Lett.* 46 (12), 6352–6362.
- Luo, Y., Liu, Z., 2019b. Slow-slip recurrent pattern changes: perturbation responding and possible scenarios of precursor toward a megathrust earthquake. *Geochem. Geophys. Geosyst.* 20 (2), 852–871.
- Ma, S., He, C., 2001. Period doubling as a result of slip complexities in sliding surfaces with strength heterogeneity. *Tectonophysics* 337 (1–2), 135–145.
- Mair, K., Marone, C., 1999. Friction of simulated fault gouge for a wide range of velocities and normal stresses. *J. Geophys. Res., Solid Earth* 104 (B12), 28899–28914.
- Mcllaskey, G.C., Yamashita, F., 2017. Slow and fast ruptures on a laboratory fault controlled by loading characteristics. *J. Geophys. Res., Solid Earth* 122 (5), 3719–3738.
- MclLaskey, G.C., Kilgore, B.D., 2013. Foreshocks during the nucleation of stick-slip instability. *J. Geophys. Res., Solid Earth* 118 (6), 2982–2997.
- Niemeijer, A.R., Vissers, R.L., 2014. Earthquake rupture propagation inferred from the spatial distribution of fault rock frictional properties. *Earth Planet. Sci. Lett.* 396, 154–164.
- Obara, K., Hirose, H., Yamamizu, F., Kasahara, K., 2004. Episodic slow slip events accompanied by non-volcanic tremors in southwest Japan subduction zone. *Geophys. Res. Lett.* 31 (23).
- Ohnaka, M., Kuwahara, Y., Yamamoto, K., Hirasawa, T., 1986. Dynamic breakdown processes and the generating mechanism for high-frequency elastic radiation during stick-slip instabilities. *Earthq. Source Mech.* 37, 13–24.
- Okubo, P.G., Dieterich, J.H., 1981. Fracture energy of stick-slip events in a large scale biaxial experiment. *Geophys. Res. Lett.* 8 (8), 887–890.
- Peng, Z., Gomberg, J., 2010. An integrated perspective of the continuum between earthquakes and slow-slip phenomena. *Nat. Geosci.* 3 (9), 599.
- Perfettini, H., Ampuero, J., 2008. Dynamics of a velocity strengthening fault region: implications for slow earthquakes and postseismic slip. *J. Geophys. Res., Solid Earth* 113 (B9).
- Ray, S., Viesca, R.C., 2017. Earthquake nucleation on faults with heterogeneous frictional properties, normal stress. *J. Geophys. Res., Solid Earth* 122 (10), 8214–8240.
- Rubin, A.M., Ampuero, J., 2005. Earthquake nucleation on (aging) rate and state faults. *J. Geophys. Res., Solid Earth* 110 (B11), B11312.
- Schaal, N., Lapusta, N., 2019. Microseismicity on patches of higher compression during larger-scale earthquake nucleation in a rate-and-state fault model. *J. Geophys. Res., Solid Earth* 124 (2), 1962–1990.
- Schmidt, D., Gao, H., 2010. Source parameters and time-dependent slip distributions of slow slip events on the Cascadia subduction zone from 1998 to 2008. *J. Geophys. Res., Solid Earth* 115 (B4).

- Schmittbuhl, J., Chambon, G., Hansen, A., Bouchon, M., 2006. Are stress distributions along faults the signature of asperity squeeze? *Geophys. Res. Lett.* 33 (13).
- Shibazaki, B., Matsuzawa, T., Tsutsumi, A., Ujiie, K., Hasegawa, A., Ito, Y., 2011. 3D modeling of the cycle of a great Tohoku-oki earthquake, considering frictional behavior at low to high slip velocities. *Geophys. Res. Lett.* 38 (21).
- Skarbek, R.M., Rempel, A.W., Schmidt, D.A., 2012. Geologic heterogeneity can produce aseismic slip transients. *Geophys. Res. Lett.* 39 (21).
- Tesei, T., Collettini, C., Barchi, M.R., Carpenter, B.M., Di Stefano, G., 2014. Heterogeneous strength and fault zone complexity of carbonate-bearing thrusts with possible implications for seismicity. *Earth Planet. Sci. Lett.* 408, 307–318.
- Thielicke, W., Stamhuis, E.J., 2014. PIVlab - Towards user-friendly, affordable and accurate digital Particle Image Velocimetry in MATLAB. *J. Open Res. Softw.* 2 (1).
- Veedu, D.M., Barbot, S., 2016. The Parkfield tremors reveal slow and fast ruptures on the same asperity. *Nature* 532 (7599), 361.
- Wallace, L.M., Webb, S.C., Ito, Y., Mochizuki, K., Hino, R., Henrys, S., Schwartz, S.Y., Sheehan, A.F., 2016. Slow slip near the trench at the Hikurangi subduction zone. *N. Z. J. For. Sci.* 352 (6286), 701–704.
- Wu, B.S., McLaskey, G.C., 2019. Contained laboratory earthquakes ranging from slow to fast. *J. Geophys. Res., Solid Earth* 124 (10), 10270–10291.
- Zecevic, M., Daniel, G., Jurick, D., 2016. On the nature of long-period long-duration seismic events detected during hydraulic fracturing on the nature of LPLD events. *Geophysics* 81 (3), KS113–KS121.
- Zhuo, Y., Liu, P., Chen, S., Guo, Y., Ma, J., 2018. Laboratory observations of tremor-like events generated during preslip. *Geophys. Res. Lett.* 45 (14), 6926–6934.